Research Article | Vol. 30, No. 21 / 10 Oct 2022 / Optics Express 38424
Optics EXPRESS

Reference shape effects on Fourier transform holography

ERIK MALM,[1,2,*] BASTIAN PFAU,[3] MICHAEL SCHNEIDER,[3] CHRISTIAN M. GÜNTHER,[4,5] PIET HESSING,[3] FELIX BÜTTNER,[6] ANDERS MIKKELSEN,[2] AND STEFAN EISEBITT[3,5]

[1]*Department of Physics, Norwegian University of Science and Technology (NTNU), Høgskoleringen 5, 7491 Trondheim, Norway*
[2]*Department of Physics, Lund University, P.O. Box 118, SE- 22100 Lund, Sweden*
[3]*Max Born Institute for Nonlinear Optics and Short Pulse Spectroscopy, Max-Born-Straße 2A, 12489 Berlin, Germany*
[4]*Technische Universität Berlin, Zentraleinrichtung Elektronenmikroskopie (ZELMI), Straße des 17. Juni 135, 10623 Berlin, Germany*
[5]*Technische Universität Berlin, Institut für Optik und Atomare Physik, Straße des 17. Juni 135, 10623 Berlin, Germany*
[6]*Helmholtz-Zentrum Berlin für Materialien und Energie GmbH, Hahn-Meitner-Platz 1, 14109 Berlin, Germany*
[*]*erikb.malm@gmail.com*

Abstract: Soft-x-ray holography which utilizes an optics mask fabricated in direct contact with the sample, is a widely applied x-ray microscopy method, in particular, for investigating magnetic samples. The optics mask splits the x-ray beam into a reference wave and a wave to illuminate the sample. The reconstruction quality in such a Fourier-transform holography experiment depends primarily on the characteristics of the reference wave, typically emerging from a small, high-aspect-ratio pinhole in the mask. In this paper, we study two commonly used reference geometries and investigate how their 3D structure affects the reconstruction within an x-ray Fourier holography experiment. Insight into these effects is obtained by imaging the exit waves from reference pinholes via high-resolution coherent diffraction imaging combined with three-dimensional multislice simulations of the x-ray propagation through the reference pinhole. The results were used to simulate Fourier-transform holography experiments to determine the spatial resolution and precise location of the reconstruction plane for different reference geometries. Based on our findings, we discuss the properties of the reference pinholes with view on application in soft-x-ray holography experiments.

1. Introduction

X-ray microscopy is an important set of techniques for studying the structure and dynamics of modern materials at the nanometer scale. However, the short wavelength and weak interaction with matter make it challenging to fabricate high-quality x-ray optics to reach a wavelength-level spatial resolution. As a consequence, a collection of coherent, lensless imaging techniques have been developed with the aim of replacing x-ray optics by numerical algorithms. The three most common methods include: holography, coherent diffractive imaging (CDI), and ptychography. Overviews on these methods are provided in Refs. [1–5].

The general difficulty associated with these lensless imaging techniques is the so-called "phase problem" which results from a detector's inability to measure a wavefront's phase. To overcome this problem, Fourier-transform holography (FTH) uses an ideally spherical reference wave,

#463338 https://doi.org/10.1364/OE.463338
Journal © 2022 Received 15 Jun 2022; revised 12 Sep 2022; accepted 19 Sep 2022; published 3 Oct 2022

Optics EXPRESS

which interferes with the wave scattered from the sample, to encode the phase into the intensity measurements. As a result, FTH is a non-iterative method that allows for a fast and deterministic reconstruction procedure. In the typical mask-based geometry for soft x-rays, the reference wave originates from a small pinhole spatially separated in the transverse direction from the sample [1,6]. A sketch of this type of experiment is shown in Fig. 1. The sample's image is recovered by applying an inverse Fourier transform to the measured intensities. Both the reference pinhole and an aperture defining the field of view for the sample are produced into a metal mask which is opaque to soft x-rays. A monolithic combination of mask and sample in a single unit makes FTH inherently insensitive to sample drifts [7,8], and provides open space around the sample allowing for various sample environments [9,10] and excitation schemes [11,12]. Combining FTH with CDI post-processing of the reconstruction even allows overcoming limitations in the spatial resolution resulting from the holography optics [13,14]. The high-resolution capability paired with the simple reconstruction procedure makes FTH a powerful technique which has been used to investigate a variety of different types of samples, including, in particular, magnetic thin films [6,11,12,15–17] and nanostructures [8,9,18] but also a free-flying virus [19], insulator-metal phase transitions [10] and meteoroid material [20].

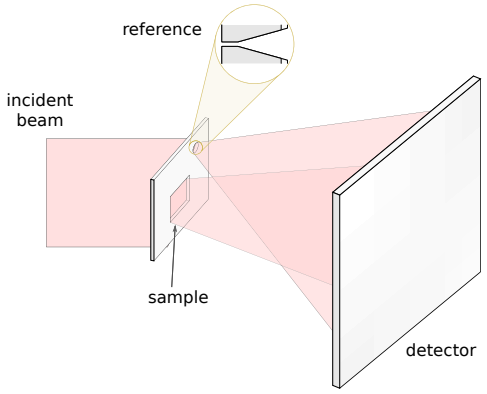

Fig. 1. The geometry (not to scale) of a mask-based FTH experiment. The sample mask splits the incident beam into sample and reference waves which diffract and interfere on the detector to produce a hologram. The cross-sectional shape of the references considered in this work is shown at the top of the image.

Roughly speaking, the image in an FTH experiment is formed by the cross-correlation between the sample's exit wave and reference wave. Smaller reference holes, thus, result in reconstructions with higher spatial resolution but also lead to lower photon throughput from the reference. Using a large reference aperture will typically increase the signal-to-noise ratio (SNR) of the image but impairs the spatial resolution. In addition, a large reference combined with a high-numerical-aperture detection system may result in contrast inversion of certain high spatial frequencies which can be corrected for by applying a free-space propagation operator to the data [21]; this, however, does not affect the transfer function's amplitude which still limits the achievable resolution. In practice, this means one must choose between either a higher SNR or improved spatial resolution. This dilemma has motivated work to develop more complicated x-ray holography geometries which can avoid this trade-off by allowing reference apertures with extended shapes [7,22–28] or by employing the focus of a Fresnel zone plate [29–31]. In essence, the former methods trade the simple but photon-limited reconstruction procedure of FTH for more complicated numerical procedures with the potential for improved SNR [3].

All of these mask-based approaches have in common that the reference beam is formed by deliberately shaped apertures in an x-ray-opaque metal film which is thick compared to the

Optics EXPRESS

smallest feature sizes of the apertures needed to achieve nanometer-scale resolution in the image reconstructions. In other words, the apertures have very high aspect ratios (longitudinal depth over lateral feature size), typically exceeding 10 by far. While the diffraction of such 3D structures cannot be approximated by their 2D lateral shape [32,33], this approximation is predominantly employed to describe holographic image formation. Moreover, once the reference aperture becomes optically thick, it is unclear which plane is being reconstructed and, as a result, the extent over which the field should be propagated to obtain an in-focus image. A precise understanding of these effects is, thus, necessary to improve reference designs and numerical algorithms to obtain reconstructions with the highest signal-to-noise and spatial resolution possible.

In this work, we focus on pinholes as the simplest reference structures and examine how the 3D shape of the reference pinhole affects the reconstruction in a soft-x-ray FTH experiment. We apply phase retrieval to high-resolution x-ray diffraction measurements to recover sample images from differently sized reference apertures produced in an identical way as for standard soft-x-ray FTH masks. This is combined with multislice simulations [34–36] to gain an understanding of how the field propagates through these structures. These simulations are used to simulate FTH experiments with different geometries to gain insight into the reconstruction procedure. A common issue related to coherent lensless imaging is identifying the reconstruction plane for thick samples or reference apertures. In contrast to CDI, where the reconstruction plane is determined by the support shape [37], the reconstruction plane in an FTH experiment is determined by the reference. The multislice simulations allow us to determine the precise location of the reconstruction plane by monitoring the total variation of the reconstruction. Moreover, these simulations reveal that, for a particular orientation, reference apertures with small opening angles can worsen the spatial resolution and should therefore be avoided.

2. Diffraction experiment

To investigate the x-ray transmission through a typical reference pinhole, we produced samples of isolated pinholes based on our standard FTH sample recipe. A silicon-nitride membrane with 200 nm thickness serves as substrate. In a typical FTH geometry, the flat surface of the membrane would support the actual sample while the holographic optics mask is produced on the membrane's backside into an x-ray-opaque metal film. For the samples considered here, we deposited 20 repeats of a Cr/Au multilayer with a layer thickness ratio of approximately 10:1 up to a total thickness of 1.85 µm as determined from atomic-force microscopy measurements.

The pinhole was produced by focused-ion-beam (FIB) milling from the silicon-nitride side in two steps. First, a conical funnel was milled that promotes material removal from the milling site. Second, the actual pinhole with the target diameter was produced straight through the remaining Cr/Au material. We produced pinholes with three nominal target diameters: 40 nm, 70 nm, and 100 nm, covering the typical range in a soft-x-ray FTH experiment. We present scanning-electron-microscope (SEM) images of the pinholes' exit at the Cr/Au side as insets in Fig. 2(d'–f'), and a cross-section of a pinhole and its conical funnel in Fig. 3(a). Although we aimed at a spherical shape of the pinholes, the actual pinholes produced show some deviation from this shape including some degree of astigmatism. These irregularities are likely caused, on the one hand, by a not fully corrected focal astigmatism of the FIB and, on the other hand, by the grain structure of the Cr/Au layer. According to the SEM images, the 100 nm pinhole matches the target size while the other two are slightly larger than targeted by 5 nm–15 nm (Table 1).

The x-ray scattering experiment was carried out at the undulator beamline P04 of the PETRA III synchrotron-radiation facility (DESY, Hamburg, Germany). The sample was placed into the beamline's focal spot of approximately 10 µm size in diameter (full-width at half maximum, fwhm) with a typical coherence length of >1 µm [38]. The photon energy was tuned to 780 eV (wavelength λ = 1.59 nm) with an energy resolution ($E/\Delta E$) better than 1×10^3 and with circular polarization. The photon energy was deliberately chosen to match typical FTH experiments on

Optics EXPRESS

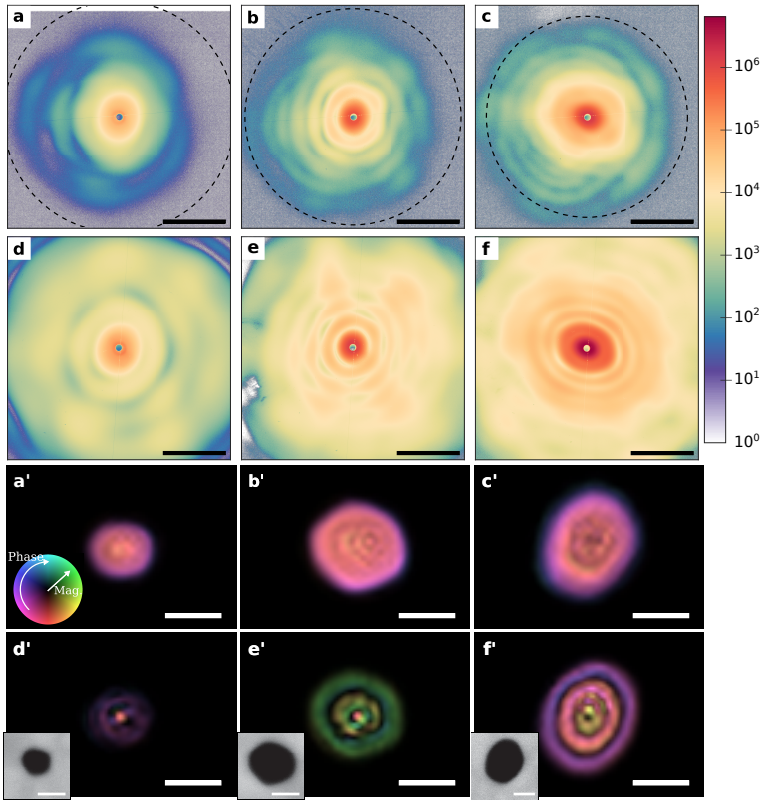

Fig. 2. (a–c) Far-field diffraction data (logarithmic pseudo-color intensity scale) from 40 nm, 70 nm and 100 nm diameter reference apertures, respectively, when the small opening (corresponding to G_{small}) was illuminated. The circular dashed line indicates the geometrically estimated opening angle of the conical section of each aperture. (d–f) Diffraction patterns from references with diameters of 40 nm, 70 nm and 100 nm, respectively, when the large opening (G_{large}) was illuminated. See Fig. 3 for layouts corresponding to G_{large} and G_{small}. The scalebars in (a–f) correspond to $50\,\mu m^{-1}$ where the spatial frequency (q) is related to the observation angle (θ) and wavelength (λ) through $q = \sin\theta/\lambda$. (a'–f') Phase retrieval reconstructions associated on the diffraction measurements from (a–f), respectively. (d'–f') Insets show SEM images of the tube openings. The scalebars in (d'–f') correspond to 50 nm. The inset in (a') shows the mapping used to visualize the complex-valued exit wave reconstructions; the magnitude and phase of the complex image are mapped to value and hue within the image respectively.

Table 1. (Three leftmost columns) Target and measured aperture diameters determined from SEM and CDI reconstruction images. The diameters were determined in an elliptical fit of the pinhole-exit circumference and given as minor and major axes. (Rightmost columns) Propagation distances necessary to refocus the reconstruction which were determined by the FTH simulations. The approximate locations of the reconstruction planes are shown by the blue dashed lines in Fig. 3(b,d).

	Diameter (minor/major) (nm)		Propagation distance (μm)	
Target	SEM	CDI	G_{large}	G_{small}
40	47/54 ± 2	51/59 ± 5	2.07	−1.5
70	75/85 ± 3	78/87 ± 5	2.08	−1.47
100	87/107 ± 3	84/100 ± 6	2.11	−1.45

Optics EXPRESS

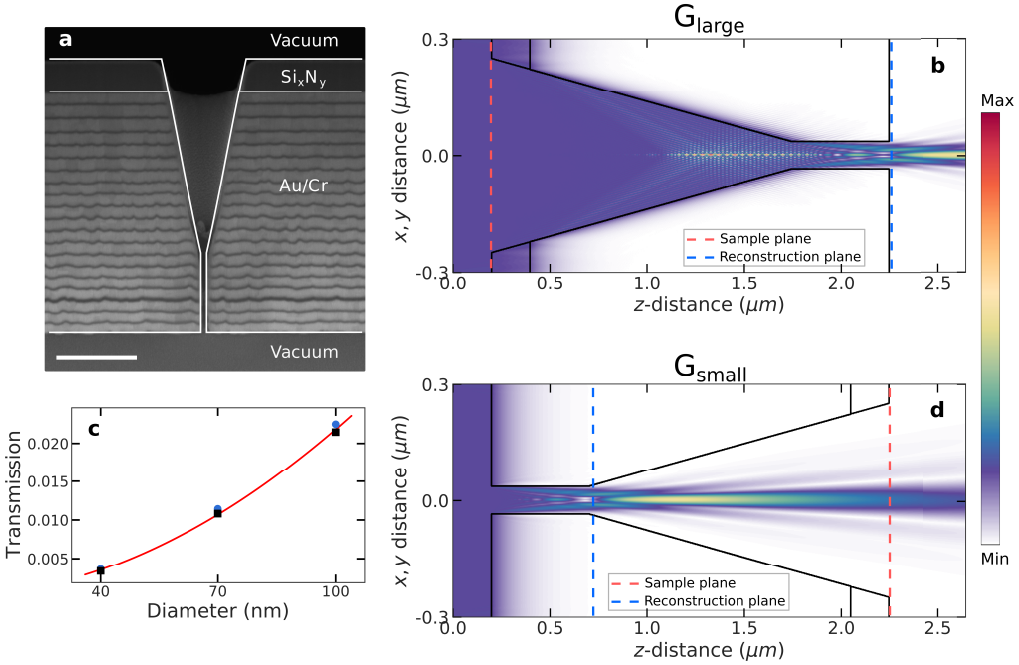

Fig. 3. (a) SEM image showing the cross-section of a 40 nm reference aperture. The white lines indicate the material boundaries. The scalebar in the lower left corner corresponds to 500 nm. (b,d) Results from the multislice simulations (reference diameter 70 nm) which show the field as it propagates through the reference aperture with the field incident from the left. The red dashed lines indicate the sample planes for the FTH simulations. The blue dashed lines show the reconstruction planes within the simulated FTH experiment. (c) The transmission percentage calculated from the multislice simulations for the two geometries G_{small} and G_{large} corresponding to the blue circles and black squares, respectively. The red line shows the ratio between the area of the smallest opening to the total area illuminated.

Co-based functional magnetic materials [6,8,9,11,12,15,16,18]. A charge-coupled device (CCD) detector with 2048 × 2048 pixels and 13.5 µm pixel size recorded the diffraction patterns in the far-field at a distance of 85 mm behind the sample. This geometry corresponds to an maximum full detection angle between 18° (CCD edge) and 25° (CCD corner). The measurements were centered and padded to 2100 × 2100 pixels. For phase retrieval, each diffraction pattern was additionally binned to a final size of 100 × 100 pixels. The binning operation was possible due to the smooth nature of the diffraction patterns, or equivalently, the large oversampling ratio [39]. In this experimental geometry, the real-space pixel size corresponds to 4.8 nm. A spherical beamstop blocked residual higher-order undulator harmonics transmitted through the Cr/Au layer.

We recorded diffraction patterns in two different orientations of the sample: in the first geometry (referred to as G_{large}), the silicon-nitride side with the large opening was illuminated first and the radiation leaves through the tube. In the second geometry (referred to as G_{small}), the Cr/Au side with the small opening was illuminated first and the radiation leaves through the conical section. Each diffraction pattern was typically assembled from 100 CCD acquisitions in order to improve its dynamic range. In Fig. 2(a–f), we compare the center portion (1800 × 1800 pixels) of the measured diffraction patterns for the pinholes with 40 nm, 70 nm and 100 nm diameter for both illumination geometries. At low diffraction angles, all diffraction patterns are characterized by an almost isotropic Airy-like pattern that quickly washes out and turns to a more disordered pattern at higher angles. The contrast between minima and maxima, i.e., the visibility,

Optics EXPRESS

is unexpectedly low although the x-ray illumination is considered to be fully coherent over such small extent ($\leq$100 nm). We, thus, attribute these deviations from the Airy diffraction pattern of a thin circular aperture to the 3D shape of the pinhole. Most remarkably, we observe significant scattering intensity up to the edge of the CCD when the large opening was illuminated while the scattering signal drastically diminishes at high scattering angles for when the small opening was illuminated.

Based on the coherent diffraction patterns, we reconstruct the reference wave at the sample exit employing iterative phase-retrieval methods. In detail, the phase was recovered by using a combination of the error-reduction (ER) and hybrid input-output (HIO) algorithms [40] for a total of 20 000 iterations. The HIO algorithm was included into the reconstruction procedure to help avoiding the estimate from stagnating near local minima. In these measurements, the size of the central speckle was significantly larger than that of the beamstop. As a result, there were no unconstrained modes [41] which allowed for a simple procedure to recover the missing data. To do this, the modulus projection was modified to update only the values lying outside the beamstop region while allowing the values to float in areas where no data was measured. The sample support was treated as a dynamic variable and updated using the method described in [42]. The method consists of two basic steps: first, the reconstruction amplitude is blurred with a Gaussian kernel. Second, the new support becomes the reconstruction region with values above a specified threshold. The reliability of the algorithm was improved by implementing a guided approach similar to the procedure described in Ref. [43] using 32 independent reconstructions. The parents for the next generation of solutions were chosen as the reconstructions that had both the smallest mismatch to the data and smallest support size. From a multi-objective perspective, these solutions comprise the Pareto front.

The interpolated reconstructions associated with the data from Fig. 2(a–f) are shown in Fig. 2(a'–f'). The value and hue of the images are used to visualize the amplitude and phase of the complex-valued reconstructions; this mapping is shown in the inset of Fig. 2(a'). The amplitude and phase components are shown separately in Fig. S1 in Supplement 1. The shape of the reconstructions are in good agreement with the SEM images of the apertures shown in the insets of Fig. 2(d'–f'). The estimated size from the CDI reconstruction also matches the SEM measurements (Table 1). Very strikingly, we find that the exit waves associated with the illumination of the large opening (G_{large}) (Fig. 2(d'–f')) contain higher spatial frequencies and larger phase variations than those corresponding to the G_{small} geometry (Fig. 2(a'–c')).

3. Multislice simulations

We numerically simulated the x-ray scattering from such apertures with high aspect ratio in order to gain insight into to the function of the apertures as source for a FTH reference wave. These simulations utilized the multislice method to propagate a plane wave through different 3D reference structures. In the multislice method, the sample's refractive index is discretized into 2D slices which are stacked along the incident field direction (z-axis). The field is propagated between slices by first transmitting the field through the slice using the projection approximation followed by free-space propagation to the entrance of the next slice. This process is repeated until the field has been propagated through the entire sample. The method is fast and is particularly well-suited for sample dimensions which are large compared to the wavelength. In this situation, finite difference, boundary integral or finite-element methods become computationally demanding. A drawback of this method is the lack of any back-scattered field. Fortunately, in the x-ray regime, the back-scattered fields are relatively small due to the small deviation of most materials' index of refraction from unity. This makes the multislice technique a good approach for simulating x-ray propagation within 3D structures. More detailed descriptions of the method are given in the treatments in Refs. [34,35,41].

Optics EXPRESS

We used SEM images of the reference pinholes to model the 3D shape and material composition for the multislice simulations. An image of the cross section of a reference pinhole is shown in Fig. 3(a). A FEI/Thermofischer Helios Nanolab 600 FIB was used to produce cross sections of the references which allow such views along the optical axis. In the image, the optical axis (z-axis) corresponds to the vertical direction. We can see that the reference is funnel-shaped consisting of a conical section followed by a smaller cylindrical tube. We model all the references with the same funnel shape consisting of a 1550 nm long conical section followed by a 500 nm long tube. The diameter of the large opening was fixed to 500 nm which corresponds to nominal full opening angles, 2θ, of 15°–17° which are slightly smaller than the CCD acceptance. The tube diameter ranges between 40 nm–100 nm. The incident field was modeled as a transverse electromagnetic plane wave directed along the z-direction. The sample was discretized using voxels with a size of 1.2 nm in the x, y-directions and 2 nm in the z-direction. The sample had no magnetic order and had large structure sizes compared to the wavelength. As a consequence, we considered only a single component of the electric field and utilized scalar diffraction theory.

4. Results

The wavefield (amplitude) as it propagates through a 70 nm reference hole is shown in Fig. 3(b,d) (see Fig. S2 in Supplement 1 for the simulation results associated with the 40 nm and 100 nm diameter references). In these images, the field is incident from the left. These simulations unveil that the transmission through pinholes of the geometry considered here can only insufficiently be approximated by a 2D model of a circular aperture. Diffraction and reflection effects clearly govern the propagation through the tubular section of the pinhole. These effects strongly modulate the field amplitude and the phase of the propagating beam. The calculated transmission through the two geometries (G_{small} and G_{large}) for different diameters is plotted in Fig. 3(c). For comparison, the red line shows the ratio between the area of the smallest opening (i.e., the tube) and the total computational area (600×600 nm^2). The agreement between this calculation and the data points from the simulation indicates that the total transmission through the pinholes is almost entirely given by geometric considerations. The transmission is marginally higher for the geometry G_{large} (Fig. 3(b)) as the larger opening within the silicon-nitride is likely able to collect slightly more light.

Next, we compare the near and far fields obtained experimentally to those obtained through numerical simulations. Figure 4(a,b) show radial plots (intensity shown on logarithmic scale) of the far-field measurements (blue) compared to multislice simulations of an 85 nm reference (gray dashed). The reference diameter in the simulation was selected to match the diffraction data. The blue line and shaded region correspond to an azimuthal average and standard deviation respectively. The multislice diffraction patterns were calculated by propagating the field through the reference aperture, followed by far-field propagation of the exit wave by 85 mm to the detector plane. We also compare these results with an analytic model (green dot-dashed) corresponding to the diffraction pattern from an infinitely thin circular opening. The time-averaged power per unit solid angle diffracted from a circular aperture is proportional to [44]

$$\frac{dP}{d\Omega} \propto \left| \frac{J_1(ka \sin\theta)}{ka \sin\theta} \right|^2, \tag{1}$$

where $k = 2\pi/\lambda$ is the wavenumber, a is the hole radius, θ is the observation angle measured relative to the optical axis and J_1 is the Bessel function of the first kind of order 1. As we needed to reduce the pinhole diameter in this model to $2a = 75$ nm to match the position of the first minima and maxima of the diffraction from the 3D pinhole structure, we conclude that the x-ray propagation through the extended tube structure reduces the effective size of the pinhole compared to the thin-aperture approximation. In addition, the propagation through the extended

Optics EXPRESS

structure leads to a blurring of the diffraction minima and, thus, to a more continuous intensity distribution without any pronounced minima, matching our observations.

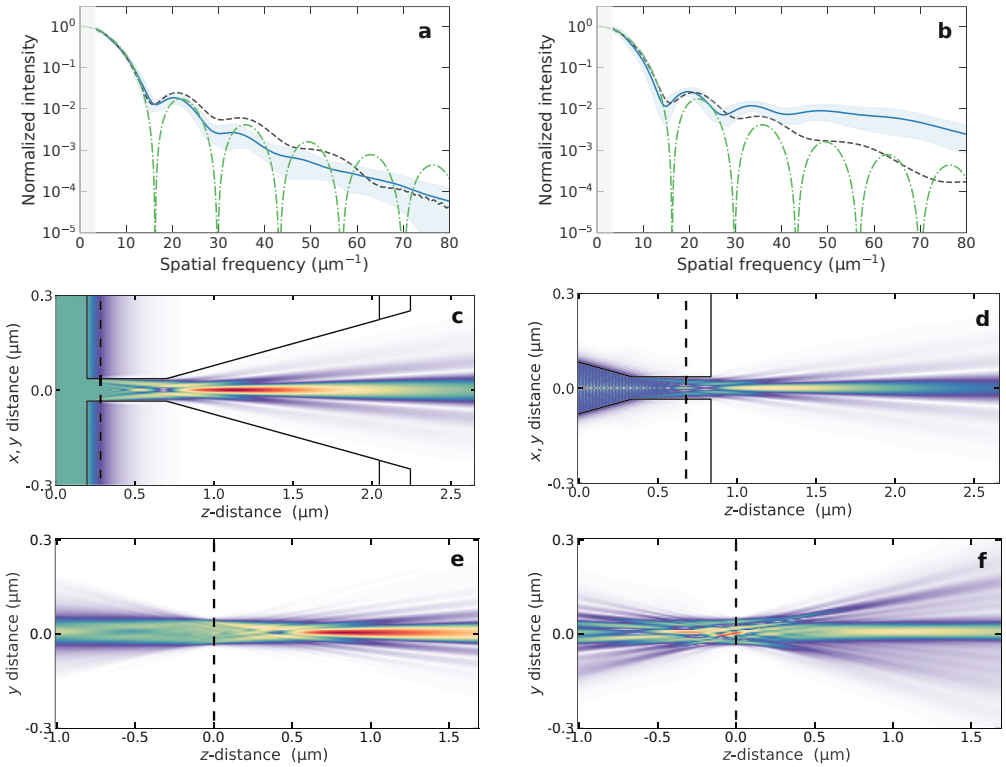

Fig. 4. Far and near-field comparisons between experiment and simulation for the (left) G_{small} and (right) G_{large} geometries respectively. (a,b) Radial plots of the far-field diffraction patterns for experimental data (blue) and simulation (dashed gray). The blue line and shaded region correspond to the azimuthal average and standard deviation respectively. An analytic solution for a circular opening with 75 nm diameter is shown by the green dashed line. The multislice simulations were calculated using a 85 nm diameter reference. The shaded regions indicate the presence of a beamstop where no experimental data is available. (c–f) Near-field comparisons between (c,d) multislice simulations and (e,f) reconstructions from Fig. 2(b',e') obtained with phase retrieval. Approximate reconstruction plane locations are indicated by the black dashed lines. The colormap used for (c–f) is the same as that from Fig. 2(b,d).

We can see from Fig. 4(a,b) that the simulations do not accurately fit the experimental signal at high spatial frequencies. Our model reproduces the observation of higher scattering intensity at high scattering angles when the large opening is illuminated. However, in the experiment, the effect is even more pronounced than predicted by the multislice simulation. Several experimental reasons could explain the differences. First, the shape of the actual reference apertures deviates from the model assuming a perfectly symmetric circular opening with straight walls inside the material. In particular, the shape model neglects any roughness of the walls of the pinhole tube, any grain structure of the Cr/Au layer, and any variation in the pinhole tube diameter which develops from the redeposition of material at the walls. Apart from the pinhole properties, it is possible that the sample is slightly tilted with respect to the incident field direction and that the incident beam deviates from a perfect plane wave. While the pinhole diameters (<100 nm) are much smaller than the x-ray beam footprint (>10 μm), partial coherence (including sample or beam vibrations) or a divergent wavefront would have an effect on the diffraction data. Lastly,

Optics EXPRESS

the simulation assumed that the sample remained unchanged during the measurement process without any carbon deposited on the sample. However, instead of tailoring the simulations to match the experiment closely, we opted to use a simplified model which allows various effects to be separated from each other and clearer insights into the method.

In Fig. 4(c–f), the near fields of multislice simulations are compared to the phase retrieval reconstructions by showing planes parallel to the propagation axis. To this end, the phase retrieval results shown in Fig. 2(b',e') were free-space propagated along the optical axis. Note that a direct comparison between simulation and experimentally obtained data is only possible in regions where the x-rays (almost) freely propagate. In particular, the fields in the leftmost regions of Fig. 4(c,d) are not related through free-space propagation due to the narrow pinhole tube. The locations of the CDI reconstruction planes, indicated by the black dashed lines, were approximated by visual comparisons between the field distribution in the simulation and the CDI reconstruction. In both orientations, the reconstructions occur in planes slightly before (150 nm–400 nm) the tube exit. It was previously found that the reconstruction plane in phase retrieval is determined by the support shape [37]. In our case, the shrinkwrap method was used to iteratively determine the support. For this reason, it is difficult to make any general arguments about the location of the reconstruction plane.

Next, multislice simulations of the reference apertures were utilized to simulate FTH experiments. These simulations allowed for the effects related to the reference aperture shape to be isolated and its influence on the reconstruction quality to be studied. A thin (one voxel thickness), laterally 1 µm large, square opening located on the outer surface of the silicon-nitride represented the sample. A thin sample was simulated to isolate the reference wave effects. The sample planes in both geometries are indicated in Fig. 3(b,d) by the red dashed lines. In the transverse direction, the reference and sample were placed 2 µm apart to satisfy the holographic separation conditions [6]. In the case where the large opening is illuminated (Fig. 3(b)), the sample wave needed to be free-space propagated to the exit surface of the sample before combining with the reference wave to create the total exit wave. In contrast, for the other geometry G_{small} (Fig. 3(d)), only the reference wave was propagated as the sample and exit planes already coincide.

Once the fields had been propagated to the sample's exit surface, they were free-space propagated to the detector plane where the intensities were "measured" by the detector. The "measurements" were calculated by taking the square of the sum of both far-field amplitudes. In order to focus on reference-related effects on the image formation, we neglected noise that could arise due to detector readout or from the stochastic nature of the field itself. Following the typical FTH reconstruction procedure, an inverse Fourier transform was applied to the intensity measurements to obtain the sample reconstruction.

The usage of a binary square as the sample is motivated by two reasons: first, the straight edges allow the knife-edge method to determine the resolution. This method extracts a line perpendicular to a straight edge within the reconstruction and defines the distance between 10 % and 90 % of the maximum amplitude as the resolution. Second, the square object allows for the reconstruction plane to be determined by monitoring the total variation of the reconstruction as a binary square has only non-zero gradients along its edges. The total variation of a function, u, is defined as the L^1-norm of the magnitude of the gradient, $TV(u) := \|\nabla u\|_{L^1}$. When the reconstruction is unfocused, ringing artifacts and smoother edges produce larger total variation values, providing a precise determination of the reconstruction plane (see Fig. S4 in Supplement 1). The results of these simulations are summarized in Fig. 5. Reconstructions before and after focusing by free-space propagation are shown in Fig. 5(a,b) for a 40 nm reference. A clear resolution improvement by free-space propagation can be seen along with the complete elimination of the fringes associated with an out-of-focus reconstruction. Knife-edge plots are shown in Fig. 5(c,d) for reconstructions before and after propagation, respectively. It is evident that refocusing the reconstruction becomes more important as the reference diameter decreases.

Optics EXPRESS

Figure 5(e) summarizes the resolution results for three reference diameters before and after focusing the reconstruction. The resolution obtained from the unfocused reconstruction does not match the reference pinhole size. In particular, for small references (cf. the data point for 40 nm diameter), focusing is absolutely necessary to reach appropriately resolved images. After focusing, the resolution reduces to values below the reference tube diameter. In the region for the reference size considered here, we find a linear relation between reference diameter d and resolution r which can be expressed by $r = 0.65(d - 10\,\text{nm})$. This relationship holds to within the precision of the numerical simulation, which in this case, is 2.6 nm. The proportionality factor is very close to the value of 0.69 which has been derived for an infinitely thin circular aperture Ref. [45]. However, a reference diameter reduced by 10 nm must be considered for a 3D tube-like reference structure. This finding directly relates to our observation of a far-field Airy disk with a size corresponding to a reduced pinhole diameter. Remarkably, our simulation shows that a tube-like 3D reference pinhole with 40 nm diameter can provide 20 nm resolution.

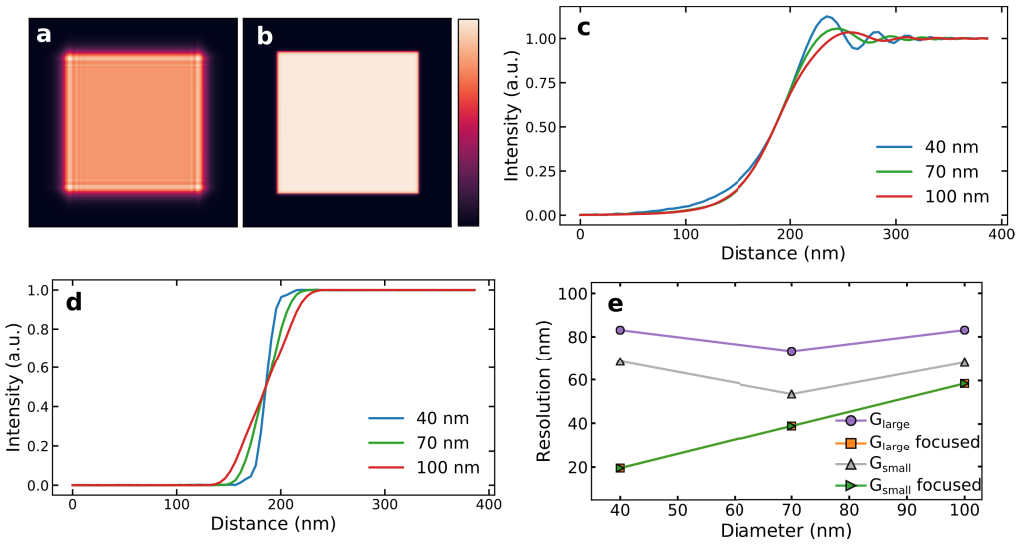

Fig. 5. The effect of refocusing on the reconstruction. (a,b) Reconstructions of the square sample with a 40 nm reference before (a) and after (b) propagation. (c,d) Knife edge cuts before and after propagation respectively which were used to determine the resolution. (e) The resolution before and after the propagation of the reconstructions for both geometries.

We do not find a difference in the resolution between the two illumination geometries once the reconstruction is propagated into the correct plane which is indicated by the complete overlap between the orange and green lines in Fig. 5(e). However, the propagation distances needed to achieve focused images differ between both geometries. The distances for the two varying diameters are summarized in Table 1. The diameters were calculated by first thresholding the images and then fitting an ellipse to the binary support. The thresholds used for converting the images into binary supports were determined using two automatic methods [46,47] implemented within scikit-image [48], and the difference between the two provided the error estimates. Remarkably, the propagation distances are almost invariant with respect to the reference diameter. From the propagation distances obtained, we are able to determine the actual FTH reconstruction plane using the sample plane as reference where the image should be in focus. In both geometries, the reconstruction planes are located immediately after the exit of the tubular part of the reference opening. This is illustrated in Fig. 3(b,d) by the blue dashed lines. The propagation distance is, thus, given only by the longitudinal distance of the sample to the reference exit and not by the

Optics EXPRESS

reference diameter. This finding contrasts a previous result for larger reference apertures (on the order of 300 nm at 3.1 nm wavelength), where focusing to the apertures first-order focal spot led to an image improvement [21]. However, this improvement was mainly associated with the correction of the sign in high-frequency bands of the imaging system's transfer function.

Lastly, we studied how the funnel's opening angle of the reference aperture affects the resolution and reconstruction plane location to study if the funnel geometry influences the imaging results as well. In this series of simulations the diameter of the exit opening was varied between 20 nm–600 nm (full size), corresponding to opening angles θ between −0.4°–10.2°. Negative values correspond to closing conical shapes. The result of the multislice simulation for a straight hole is shown in Fig. S3 in Supplement 1. The geometry of the reference structure and the results of this simulation – location of the reconstruction plane and the spatial resolution – are shown in Fig. 6. We find two different regimes depending on the opening angle. There is a region up to 3° where the reconstruction plane transitions from the sample's exit surface to the exit of the tubular part of the aperture located approximately 1.5 µm away. At the same time, the resolution first deteriorates by a factor of three from approximately 20 nm to over 60 nm and then again decreases. In this region, the diffracted field interacts strongly with the walls of the funnel leading to the effect of an artificially larger reference. The vertical dashed line at 2.8° indicates the angle (θ_1) associated with the first zero of $J_1(ka\sin\theta)$, i.e., the size of the Airy disk for a thin pinhole of the same size as the tube would produce. In the region with larger angles than θ_1 the interaction between the field and the walls becomes negligible and the propagation of the field is nearly equivalent to free-space propagation. Naturally, this regime where the resolution is independent of the funnel opening is preferred for the fabrication of FTH reference structures. Of course, this minimum opening has to be adapted to the actual divergence of the Airy disk which is related to the tube diameter (here, 40 nm).

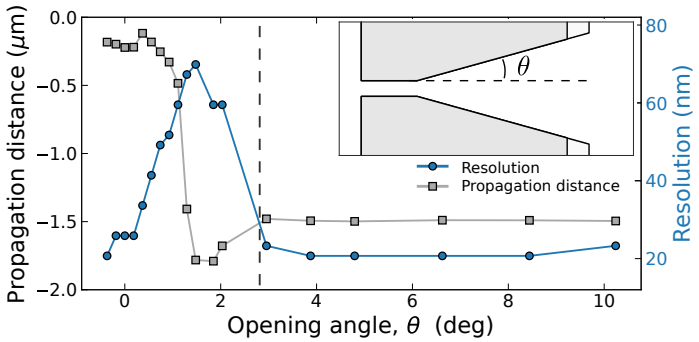

Fig. 6. Resolution (blue) and propagation distance (gray) for different opening angles. In the simulations the x-rays illuminate the small opening (G_{small}) in the Au surface. This corresponds to the geometry shown in the inset with the field incident from the left. The vertical dashed line indicates the angle (2.8°) associated with the first zero of $J_1(ka\sin\theta)$.

5. Discussion

In the following, we summarize and discuss our experimental and simulation results with particular view on the application of optically thick reference apertures in FTH experiments.

We have investigated the x-ray propagation through such an optical element by high-resolution scattering and imaging. Our detection geometry provided a numerical aperture corresponding to sub-5-nm resolution in order to be able to resolve the internal real-space structure of the wavefield exiting the pinhole. In the diffraction patterns, this corresponds to the detection of higher-order diffraction far beyond the central zero-order intensity maximum. We find these

Optics EXPRESS

higher orders significantly distorted from the classical Airy diffraction of a circular aperture, witnessing the influence of the pinhole's 3D shape on the x-ray propagation. An FTH detection geometry, however, is optimized by matching the detector's numerical aperture with the size of the central Airy disk of the reference beam while higher orders are omitted. As shown in Ref. [21], the detection of higher reference-beam orders even can lead to imaging artifacts if the FTH transfer function is not taken into account. As one of the main results of this study, we find that tubular-shaped pinholes are very well suited as reference-beam source for FTH experiments. While we give more details below, the most intuitive reason for this finding is our observation that the pinhole's zero-order diffraction coincides well with an Airy disk pattern, albeit corresponding to an apparently smaller pinhole diameter. In a complementary way to Ref. [21], we show that the spatial resolution reached in FTH-based imaging is directly related to the size of the Airy disk.

The particular 3D shape of the pinhole reference we used is motivated by two main aspects: first, its functionality for FTH implies that the layer for the metal mask (here Cr/Au) has to be thick enough (>1 µm) to fully block the soft x-ray radiation including higher harmonics of the fundamental wavelength which are typically present at synchrotron-radiation beamlines. At the same time, a reference opening on the order of some tens of nanometers is required for state-of-the-art x-ray imaging. Second, the ability to produce pinholes with such high aspect ratio via FIB involves concepts for efficient material removal. As a result, reference pinholes with high aspect ratio for soft-x-ray FTH are produced as a combination of a funnel structure followed by a tube defining the smallest opening.

We observe that the propagation of soft x-rays through such a structure is determined primarily by the tube section. Consequentially, also the orientation, i.e., the propagation direction through the structure hardly plays a role in the implementation of a FTH experiment. In particular, we find:

1. The total x-ray transmission through the reference structure is almost equal for both orientations and given by the geometric acceptance of the tube section.

2. For the wavelength and geometry used in our experiments, the achievable resolution is equal for both orientations and proportional to the tube diameter reduced by 10 nm. If the edge criterion (10 %–90 %) is employed, the proportionality factor is 0.65, being close to the value for an infinitely thin aperture. This factor can be different if alternative criteria for the resolution are employed. However, the reduced apparent diameter still applies as witnessed by the larger size of the Airy disk, detected in the far field. We note that the particular amount of the size reduction is most likely dependent on the wavelength of the x-rays used and the length of the pinhole tube.

3. In both orientations, the FTH reconstruction plane is located directly at the exit of the tube section. In particular, the position of the reconstruction plane does not depend on the pinhole diameter. One has to refocus, i.e., free-space propagate the reconstructed image to the sample plane in order to achieve an appropriate resolution corresponding to the size of the reference pinhole. Refocusing becomes more important for smaller references and for larger reconstruction plane to sample plane distances.

4. The reference's conical section only influences the FTH experiment if the x-ray radiation leaves the reference through the funnel (G_{small}). In this case, the funnel opening has to be wide enough that, at least, the central diffraction maximum can freely propagate to the detector. This finding again underlines that only the Airy disk of the reference diffraction contributes to the image formation in FTH.

In our experiments, we observe that tube-like references produce a scattering pattern that does not resemble a classical Airy pattern produced by an infinitely thin aperture. However, our

Optics EXPRESS

simulations show that the irregular far-field diffraction particularly at high scattering angles does not affect the image formation as long as the Airy disk is still sufficiently established. Having said that, the broadly distributed reference diffraction observed may be of high advantage for the combination of FTH with CDI methods. The scattering to high angles is particularly strong in the case where the beam enters from the funnel side (G_{large}). It was reported previously that the stability and convergence of the numerical iterative phase retrieval benefit from the interference with a reference wave [13,14,49–52]. In order to cover a large part of the Fourier space, this interference is promoted by a smooth diffraction intensity from the reference without pronounced minima, as observed here for the tube references. Strong reference scattering particularly at high scattering angles additionally leads to a coherent amplification of the diffraction signal from the sample and, thus, higher SNR of the CDI reconstructions paired with better spatial resolution [13,50–53].

6. Conclusions

In conclusion, we have studied the impact that the 3D shape of an optically thick reference pinhole has on the reconstruction in a soft-x-ray FTH experiment. The particular shape of the pinhole is motivated by standard designs already used in FTH implementations. Using CDI reconstructions of the pinholes' exit wave combined with multislice simulations, we find that this design is well suited for application in FTH as it provides flexibility paired with easy control of its properties. In particular, the references' transmission and achievable resolution are determined mostly by the diameter of the pinhole's tubular section and are nearly independent of the orientation of the pinhole with respect to the x-ray propagation direction. The FTH experiment particularly benefits from the property that the transmission is related to the full geometrical acceptance while the resolution provided is related to a reduced tube diameter. For our situation (1.59 nm x-ray wavelength, 500 nm tube length, 40 nm–100 nm tube diameter), we find a size reduction by 10 nm which is a considerable amount in the case of a 40 nm-sized reference pinhole.

Moreover, our study demonstrates that multislice simulations are a reliable, valuable and convenient tool to theoretically investigate the function of holographic reference aperture and nanometer-scale x-ray optics in general, in the size regime considered here. This kind of very inexpensive simulations allows for a systematic and broad screening of different shapes and geometries for x-ray optics which will likely lead to further improvements in their imaging properties.

Funding. Helmholtz Young Investigator Group Program (VH-NG-1520); Vetenskapsrådet; NanoLund, Lunds Universitet.

Acknowledgments. We acknowledge DESY (Hamburg, Germany), a member of the Helmholtz Association HGF, for the provision of experimental facilities. Parts of this research were carried out at PETRA III using beamline P04.

Disclosures. The authors declare no conflicts of interest.

Data Availability. Data underlying the results presented in this paper are not publicly available at this time but may be obtained from the authors upon reasonable request.

Supplemental document. See Supplement 1 for supporting content.

References

1. J. Goodman, *Introduction to Fourier Optics*, McGraw-Hill physical and quantum electronics series (W. H. Freeman, 2005).
2. H. N. Chapman and K. A. Nugent, "Coherent lensless x-ray imaging," Nat. Photonics **4**(12), 833–839 (2010).
3. B. Pfau and S. Eisebitt, "X-ray holography," in *Synchrotron Light Sources and Free-Electron Lasers: Accelerator Physics, Instrumentation and Science Applications*, E. Jaeschke, S. Khan, J. R. Schneider, and J. B. Hastings, eds. (Springer International Publishing, 2014), pp. 1–36.
4. J. Miao, T. Ishikawa, I. K. Robinson, and M. M. Murnane, "Beyond crystallography: Diffractive imaging using coherent x-ray light sources," Science **348**(6234), 530–535 (2015).
5. Y. Shechtman, Y. C. Eldar, O. Cohen, H. N. Chapman, J. Miao, and M. Segev, "Phase retrieval with application to optical imaging: A contemporary overview," IEEE Signal Process. Mag. **32**(3), 87–109 (2015).

Optics EXPRESS

6. S. Eisebitt, J. Lüning, W. F. Schlotter, M. Lörgen, O. Hellwig, W. Eberhardt, and J. Stöhr, "Lensless imaging of magnetic nanostructures by x-ray spectro-holography," Nature **432**(7019), 885–888 (2004).
7. J. Geilhufe, B. Pfau, M. Schneider, F. Büttner, C. M. Günther, S. Werner, S. Schaffert, E. Guehrs, S. Frömmel, M. Kläui, and S. Eisebitt, "Monolithic focused reference beam x-ray holography," Nat. Commun. **5**(1), 3008 (2014).
8. F. Büttner, C. Moutafis, M. Schneider, B. Krüger, C. M. Günther, J. Geilhufe, C. V. Schmising, J. Mohanty, B. Pfau, S. Schaffert, A. Bisig, M. Foerster, T. Schulz, C. A. Vaz, J. H. Franken, H. J. Swagten, M. Kläui, and S. Eisebitt, "Dynamics and inertia of skyrmionic spin structures," Nat. Phys. **11**(3), 225–228 (2015).
9. B. Pfau, C. M. Günther, E. Guehrs, T. Hauet, T. Hennen, S. Eisebitt, and O. Hellwig, "Influence of stray fields on the switching-field distribution for bit-patterned media based on pre-patterned substrates," Appl. Phys. Lett. **105**(13), 132407 (2014).
10. L. Vidas, C. M. Günther, T. A. Miller, B. Pfau, D. Perez-Salinas, E. Martínez, M. Schneider, E. Gührs, P. Gargiani, M. Valvidares, R. Marvel, K. A. Hallman, R. F. Haglund, S. Eisebitt, and S. Wall, "Imaging nanometer phase coexistence at defects during the insulator-metal phase transformation in vo2 thin films by resonant soft x-ray holography," Nano Lett. **18**(6), 3449–3453 (2018).
11. F. Büttner, I. Lemesh, M. Schneider, B. Pfau, C. M. Günther, P. Hessing, J. Geilhufe, L. Caretta, D. Engel, B. Krüger, J. Viefhaus, S. Eisebitt, and G. S. D. Beach, "Field-free deterministic ultrafast creation of magnetic skyrmions by spin-orbit torques," Nat. Nanotechnol. **12**(11), 1040–1044 (2017).
12. K. Gerlinger, B. Pfau, F. Büttner, M. Schneider, L.-M. Kern, J. Fuchs, D. Engel, C. M. Günther, M. Huang, I. Lemesh, L. Caretta, A. Churikova, P. Hessing, C. Klose, C. Strüber, C. v. K. Schmising, S. Huang, A. Wittmann, K. Litzius, D. Metternich, R. Battistelli, K. Bagschik, A. Sadovnikov, G. S. D. Beach, and S. Eisebitt, "Application concepts for ultrafast laser-induced skyrmion creation and annihilation," Appl. Phys. Lett. **118**(19), 192403 (2021).
13. S. Zayko, O. Kfir, M. Heigl, M. Lohmann, M. Sivis, M. Albrecht, and C. Ropers, "Ultrafast high-harmonic nanoscopy of magnetization dynamics," Nat. Commun. **12**(1), 6337 (2021).
14. A. S. Johnson, J. V. Conesa, L. Vidas, D. Perez-Salinas, C. M. Günther, B. Pfau, K. A. Hallman, R. F. Haglund, S. Eisebitt, and S. Wall, "Quantitative hyperspectral coherent diffractive imaging spectroscopy of a solid-state phase transition in vanadium dioxide," Sci. Adv. **7**(33), eabf1386 (2021).
15. C. Tieg, E. Jiménez, J. Camarero, J. Vogel, C. Arm, B. Rodmacq, E. Gautier, S. Auffret, B. Delaup, G. Gaudin, B. Dieny, and R. Miranda, "Imaging and quantifying perpendicular exchange biased systems by soft x-ray holography and spectroscopy," Appl. Phys. Lett. **96**(7), 072503 (2010).
16. T. A. Duckworth, F. Y. Ogrin, G. Beutier, S. S. Dhesi, S. A. Cavill, S. Langridge, A. Whiteside, T. Moore, M. Dupraz, F. Yakhou, and G. van der Laan, "Holographic imaging of interlayer coupling in co/pt/NiFe," New J. Phys. **15**(2), 023045 (2013).
17. O. Kfir, S. Zayko, C. Nolte, M. Sivis, M. Möller, B. Hebler, S. S. P. K. Arekapudi, D. Steil, S. Schäfer, M. Albrecht, O. Cohen, S. Mathias, and C. Ropers, "Nanoscale magnetic imaging using circularly polarized high-harmonic radiation," Sci. Adv. **3**(12), 1 (2017).
18. S. Streit-Nierobisch, D. Stickler, C. Gutt, L.-M. Stadler, H. Stillrich, C. Menk, R. Frömter, C. Tieg, O. Leupold, H. P. Oepen, and G. Grübel, "Magnetic soft x-ray holography study of focused ion beam-patterned co/pt multilayers," J. Appl. Phys. **106**(8), 083909 (2009).
19. T. Gorkhover, A. Ulmer, K. Ferguson, M. Bucher, F. R. N. C. Maia, J. Bielecki, T. Ekeberg, M. F. Hantke, B. J. Daurer, C. Nettelblad, J. Andreasson, A. Barty, P. Bruza, S. Carron, D. Hasse, J. Krzywinski, D. S. D. Larsson, A. Morgan, K. Mühlig, M. Müller, K. Okamoto, A. Pietrini, D. Rupp, M. Sauppe, G. van der Schot, M. Seibert, J. A. Sellberg, M. Svenda, M. Swiggers, N. Timneanu, D. Westphal, G. Williams, A. Zani, H. N. Chapman, G. Faigel, T. Möller, J. Hajdu, and C. Bostedt, "Femtosecond x-ray fourier holography imaging of free-flying nanoparticles," Nat. Photonics **12**(3), 150–153 (2018).
20. R. Blukis, B. Pfau, C. M. Günther, P. Hessing, S. Eisebitt, J. Einsle, and R. J. Harrison, "Nanoscale imaging of high-field magnetic hysteresis in meteoritic metal using x-ray holography," Geochem., Geophys., Geosyst. **21**(8), e2020GC009044 (2020).
21. J. Geilhufe, B. Pfau, C. M. Günther, M. Schneider, and S. Eisebitt, "Achieving diffraction-limited resolution in soft-x-ray fourier-transform holography," Ultramicroscopy **214**, 113005 (2020).
22. W. F. Schlotter, R. Rick, K. Chen, A. Scherz, J. Stöhr, J. Lüning, S. Eisebitt, C. Günther, W. Eberhardt, O. Hellwig, and I. McNulty, "Multiple reference fourier transform holography with soft x rays," Appl. Phys. Lett. **89**(16), 163112 (2006).
23. S. Podorov, K. Pavlov, and D. Paganin, "A non-iterative reconstruction method for direct and unambiguous coherent diffractive imaging," Opt. Express **15**(16), 9954–9962 (2007).
24. M. Guizar-Sicairos and J. R. Fienup, "Holography with extended reference by autocorrelation linear differential operation," Opt. Express **15**(26), 17592–17612 (2007).
25. S. Marchesini, S. Boutet, A. E. Sakdinawat, M. J. Bogan, S. Bajt, A. Barty, H. N. Chapman, M. Frank, S. P. Hau-Riege, A. Szöke, C. Cui, D. A. Shapiro, M. R. Howells, J. C. H. Spence, J. W. Shaevitz, J. Y. Lee, J. Hajdu, and M. M. Seibert, "Massively parallel x-ray holography," Nat. Photonics **2**(9), 560–563 (2008).
26. B. Pfau, C. M. Günther, S. Schaffert, R. Mitzner, B. Siemer, S. Roling, H. Zacharias, O. Kutz, I. Rudolph, R. Treusch, and S Eisebitt, "Femtosecond pulse x-ray imaging with a large field of view," New J. Phys. **12**(9), 095006 (2010).
27. A. V. Martin, A. J. D'Alfonso, F. Wang, R. Bean, F. Capotondi, R. A. Kirian, E. Pedersoli, L. Raimondi, F. Stellato, C. H. Yoon, and H. N. Chapman, "X-ray holography with a customizable reference," Nat. Commun. **5**(1), 4661 (2014).

Optics EXPRESS

28. C. M. Günther, E. Guehrs, M. Schneider, B. Pfau, C. von Korff Schmising, J. Geilhufe, S. Schaffert, and S. Eisebitt, "Experimental evaluation of signal-to-noise in spectro-holography via modified uniformly redundant arrays in the soft x-ray and extreme ultraviolet spectral regime," J. Opt. **19**(6), 064002 (2017).
29. I. McNulty, J. Kirz, C. Jacobsen, E. H. Anderson, M. R. Howells, and D. P. Kern, "High-resolution imaging by fourier transform x-ray holography," Science **256**(5059), 1009–1012 (1992).
30. E. B. Malm, N. C. Monserud, C. G. Brown, P. W. Wachulak, H. Xu, G. Balakrishnan, W. Chao, E. Anderson, and M. C. Marconi, "Tabletop single-shot extreme ultraviolet fourier transform holography of an extended object," Opt. Express **21**(8), 9959–9966 (2013).
31. S. Wang, A. Rockwood, Y. Wang, W.-L. Chao, P. Naulleau, H. Song, C. S. Menoni, M. Marconi, and J. J. Rocca, "Single-shot large field of view fourier transform holography with a picosecond plasma-based soft x-ray laser," Opt. Express **28**(24), 35898–35909 (2020).
32. C. Fuhse and T. Salditt, "Propagation of x-rays in ultra-narrow slits," Opt. Commun. **265**(1), 140–146 (2006).
33. S. Zayko, E. Mönnich, M. Sivis, D.-D. Mai, T. Salditt, S. Schäfer, and C. Ropers, "Coherent diffractive imaging beyond the projection approximation: waveguiding at extreme ultraviolet wavelengths," Opt. Express **23**(15), 19911–19921 (2015).
34. J. M. Cowley and A. F. Moodie, "The scattering of electrons by atoms and crystals. I. A new theoretical approach," Acta Crystallogr. **10**(10), 609–619 (1957).
35. K. Li, M. Wojcik, and C. Jacobsen, "Multislice does it all-calculating the performance of nanofocusing x-ray optics," Opt. Express **25**(3), 1831–1846 (2017).
36. P. R. T. Munro, "Rigorous multi-slice wave optical simulation of x-ray propagation in inhomogeneous space," J. Opt. Soc. Am. A **36**(7), 1197–1208 (2019).
37. J. C. H. Spence, U. Weierstall, and M. Howells, "Phase recovery and lensless imaging by iterative methods in optical, x-ray and electron diffraction," Philos. Trans. R. Soc., A **360**(1794), 875–895 (2002).
38. K. Bagschik, J. Wagner, R. Buß, M. Riepp, A. Philippi-Kobs, L. Müller, J. Buck, F. Trinter, F. Scholz, J. Seltmann, M. Hoesch, J. Viefhaus, G. Grübel, H. P. Oepen, and R. Frömter, "Direct 2d spatial-coherence determination using the fourier-analysis method: multi-parameter characterization of the p04 beamline at petra iii," Opt. Express **28**(5), 7282–7300 (2020).
39. J. Miao and D. Sayre, "On possible extensions of x-ray crystallography through diffraction-pattern oversampling," Acta Crystallogr., Sect. A: Found. Crystallogr. **56**(6), 596–605 (2000).
40. J. R. Fienup, "Phase retrieval algorithms: a comparison," Appl. Opt. **21**(15), 2758–2769 (1982).
41. P. Thibault, V. Elser, C. Jacobsen, D. Shapiro, and D. Sayre, "Reconstruction of a yeast cell from X-ray diffraction data," Acta Crystallogr., Sect. A: Found. Crystallogr. **62**(4), 248–261 (2006).
42. S. Marchesini, H. He, H. N. Chapman, S. P. Hau-Riege, A. Noy, M. R. Howells, U. Weierstall, and J. C. H. Spence, "X-ray image reconstruction from a diffraction pattern alone," Phys. Rev. B **68**(14), 140101 (2003).
43. C.-C. Chen, J. Miao, C. W. Wang, and T. K. Lee, "Application of optimization technique to noncrystalline x-ray diffraction microscopy: Guided hybrid input-output method," Phys. Rev. B **76**(6), 064113 (2007).
44. J. D. Jackson, *Classical electrodynamics* (Third edition. New York : Wiley, 1999).
45. W. Schlotter, "Lensless fourier transform holography with soft x-rays," Ph.D. thesis, Stanford University (2007).
46. N. Otsu, "A threshold selection method from gray-level histograms," IEEE Transactions on Systems, Man, and Cybernetics **9**(1), 62–66 (1979).
47. C. Li and P. Tam, "An iterative algorithm for minimum cross entropy thresholding," Pattern Recognit. Lett. **19**(8), 771–776 (1998).
48. S. van der Walt, J. L. Schönberger, J. Nunez-Iglesias, F. Boulogne, J. D. Warner, N. Yager, E. Gouillart, and T. Yu, "scikit-image: image processing in python," PeerJ **2**, e453 (2014).
49. S. Flewett, C. M. Günther, C. von Korff Schmising, B. Pfau, J. Mohanty, F. Büttner, M. Riemeier, M. Hantschmann, M. Kläui, and S. Eisebitt, "Holographically aided iterative phase retrieval," Opt. Express **20**(28), 29210–29216 (2012).
50. P. Hessing, B. Pfau, E. Guehrs, M. Schneider, L. Shemilt, J. Geilhufe, and S. Eisebitt, "Holography-guided ptychography with soft x-rays," Opt. Express **24**(2), 1840–1851 (2016).
51. C. Kim, Y. Kim, C. Song, S. S. Kim, S. Kim, H. C. Kang, Y. Hwu, K.-D. Tsuei, K. S. Liang, and D. Y. Noh, "Resolution enhancement in coherent x-ray diffraction imaging by overcoming instrumental noise," Opt. Express **22**(23), 29161–29169 (2014).
52. C.-F. Huang, W.-H. Chang, T.-K. Lee, Y. Joti, Y. Nishino, T. Kimura, A. Suzuki, Y. Bessho, T.-T. Lee, M.-C. Chen, S.-M. Yang, Y. Hwu, S.-H. Huang, P.-N. Li, P. Chen, Y.-C. Tseng, C. Ma, T.-L. Hsu, C.-H. Wong, K. Tono, T. Ishikawa, and K. S. Liang, "XFEL coherent diffraction imaging for weakly scattering particles using heterodyne interference," AIP Adv. **10**(5), 055219 (2020).
53. S. Boutet, M. J. Bogan, A. Barty, M. Frank, W. H. Benner, S. Marchesini, M. M. Seibert, J. Hajdu, and H. N. Chapman, "Ultrafast soft X-ray scattering and reference-enhanced diffractive imaging of weakly scattering nanoparticles," J. Electron Spectrosc. Relat. Phenom. **166-167**, 65–73 (2008).